Quantum Efficiency Calibration of HRC-S

R. P. Kraft

1 HRC-S Quantum Efficiency

1.1 Introduction

The quantum efficiency (QE) of the HRC-S as a function of energy and position was determined by combining data from three distinct datasets/sets of measurements. These are the XRCF HRMA+HRC-S effective area (EA) measurements, flat fields (FF) made in the HRC laboratory at SAO after XRCF, and synchrotron measurements of non-flight CsI coated MCPs around the I and Cs M edges made at the Daresbury Synchrotron Radiation Source. The first two of these were made with the flight instrument, but only the SAO flat fields were made with the instrument in the flight configuration. As described in section TBD, electronic modifications were made to the flight instrument after the XRCF measurements which significantly changed its performance. An energy (and position) dependent correction factor must be applied to all XRCF QEs to extrapolate them to the current flight configuration. Flat field measurements were taken in both the XRCF and current flight configurations, so that the effect of the electronic changes is calibrated. The third set of data, the synchrotron measurements, were not taken with the flight instrument at all, but with flight-like CsI-coated MCPs. There was no cross-calibration made between the plates taken to the synchrotron and the flight instrument, so there is considerable systematic uncertainty when extrapolating the synchrotron results to the flight instrument.

Our general procedure for determining the HRC-S QE as a function of position and energy has been to first determine the MCP QE (i.e. the QE of the flight CsI coated MCPs *without* the UVIS) at normal incidence to the MCP surface as a function of energy in a region around zeroth order at a discrete number of data points. We have used data from the XRCF and SAO FF measurements. These were all made with the UVIS, so the transmission of the shield must be divided out. As described in section TBD, the transmission and spatial uniformity of the UVIS have been well calibrated, so this adds negligible uncertainty. An interpolation algorithm based on the X-ray absorption of CsI is used to extend the HRC-S QE to a finer energy grid between the measurement energies. The synchrotron data around the Cs and I M edges are then incorporated, and the MCP QE is derated by a small factor to correct for the angular dependence of the QE on the HRMA cone angles. This MCP QE is then multiplied by the transmission of the UVIS to determine the HRC-S QE in zeroth order.

There are three additional factors that are considered to determine the spatial and dispersive (for the LETG) energy dependence of the HRC-S QE. First, based on SAO FF measurements, the MCP QE of each of the wing segments is $\sim$10% lower than that of the central segment. Second, there is a slight gradient in QE within each segment. The QE increases with increasing V coordinate (along the dispersion axis) within a given segment. The pattern of QE variation over the entire HRC-S is therefore a sawtooth. The QE variation across a given segment is $\sim$10% and is well described by a linear function. Third, the UVIS has a complex shape that must be taken into account. The HRC-S QE at the location of the nth dispersed order of the LETG is then computed.

The final data products that we present include the MCP QE and HRC-S QE in zeroth order, and the dispersed HRC-S QE in the 1st, 3rd, and 5th orders of the LETG. Each step outlined above is described in more detail in below. We also present a qualitative discussion of uncertainties and describe what additional QE measurements will be made in the HRC laboratory and as part of the on-orbit calibration plan.

We have very little data on the HRC-S QE below 277 eV, and the data that we do have is not self consistent. We therefore regard the instrument to be uncalibrated below ~250 eV. None of the plots or data tables contained in this report will contain information below 250 eV. We hope to address this problem in detail once CXO is in orbit. Several of the targets in our on-orbit calibration program were selected specifically to measure the QE in this bandpass.

1.2 The XRCF and SAO Flat Field QE Measurements

1.2.1 XRCF Effective Area Measurements

The effective area (EA) of the HRC-S + HRMA was measured at 57 energies at a position near zeroth order at the XRCF. The details of the experimental setup and measurements at XRCF are contained elsewhere (Patnaude *et al.*, 1998), and will not be repeated here. The HRC-S QE can be determined by dividing out the effective area of the HRMA. We have used the XRCF HRMA model of May 1999, and the Mission Support Team (MST) Beam Normalization Detectors (BNDs) QEs of September 1998. The QE of the instrument changed considerably after the electronic modifications, so a multiplicative correction factor must be applied to all XRCF data to extend it to the flight configuration. This is described in more detail below. In addition, the incident angle dependence of the MCP QE must also be considered when comparing or combining the XRCF data and the SAO FF data. All XRCF data was taken with the HRMA, while all SAO FF data was taken at normal incidence to the MCP surface. This correction is less than 1% above 400 eV, but at lower energies is significant.

Most of the XRCF data was taken using the double crystal monochromator (DCM) or the High Resolution Erect Field Spectrometer (HIREFS) source. A few measurements were made with an electron impact source (EIPS) around zeroth order. In general, the systematic uncertainties associated with the DCM data are small. Higher order contamination is small, and the beam was relatively uniform across the HRMA. We regard the data taken with the DCM as the best available data above 2 keV. They agree to within ~10% with the SAO FF measurements in this bandpass. These variations provide an estimate of the overall systematic uncertainty of the calibration above 2 keV. Only one EIPS measurement (at 277 eV) is used in this analysis.

The HIREFS source was used for EA measurements in the 400 eV to 2000 eV bandpass. There are two complexities of this source that make analysis and interpretation of the data much more difficult than either the DCM or the EIPS. First, this source displayed gross non-uniformities across the HRMA, as much as a factor of 3 in some cases. Second, spectral contamination from tungsten M lines around 1.7 keV as well as higher orders of the nominal calibration energy provide considerable complication given that the HRC very poor intrinsic energy resolution. The systematic uncertainties associated with data taken using this source are considerably higher than for either the EIPS or DCM. The quality of this data gets progressively worse toward the lower end of the bandpass. We have used the HIREFS data above 1.5 keV in our modeling of the HRC-S QE. Below 1.5 keV, both the statistical and systematic uncertainties become large. We have only used the HIREFS data in this bandpass for qualitative comparison with the absorption model.

1.2.2 SAO Flat Field Quantum Efficiency and Detector Uniformity Measurements

Flat field measurements were made in the HRC laboratory before and after the electronic modifications to measure the HRC-S QE in the flight configuration, the uniformity of the detector, and the effect of the electronic changes on QE. A schematic diagram of the experimental setup is given in Figure 1. The HRC-S was attached to a vacuum pipe by a mechanical snout which ensured that only one segment was illuminated at any time, and the High Energy Suppresion Filter (HESF) was blocked by a mechanical paddle. X-rays were generated by a multi-anode electron impact source. Beam filters were inserted at the source to reduce the flux and remove continuum contamination. The count rate in the instrument was typically ~1200 cts/s. The central segment

Line	Energy	Filter	Thickness (MFPs)	V_A	L/C	Seg
B K_α	183 eV	7 μm parylene-C	5.87	600 V	48.4	-1,0,+1
C K_α	277 eV	33 μm polypropylene	5.94	1000 V	171	-1,0,+1
O K_α	525 eV	2 μm Cr	4.67	1000 V	29.3	-1,0,+1
Ni L_α	851 eV	2 μm Cu	3.80	2500 V	2.55	0
Al K_α	1487 eV	50 μm Al	5.40	4000 V	38.9	-1,0,+1
Ag L_α	2984 eV	10 μm Ag	4.86	6000 V	0.60	0
Ti K_α	4511 eV	150 μm Ti	6.80	10000 V	6.73	0
Fe K_α	6404 eV	125 μm Fe	6.97	10000 V	1.78	0

Table 1: Summary of line energies, filters, thicknesses (in mean free paths at the characteristic line), anode voltages, and predicted line-to-continuum ratio of the X-ray source for HRC-S flat field measurements.

was calibrated at 8 energies, and each of the wings segments at 4. A summary of the flat field calibrations is contained in Table 1. Measurements were also made of the reflectivity of the HESF by illuminating the flat and blocking the direct beam onto the detector with a mechanical paddle. The Ag L flat field was not used in this analysis because of large non-uniformities in the beam and the complex L series spectrum centered around the Ar K edge of the proportional counter gas.

Surface plots and projections of the flat fields for the flight configuration at Al K_α for segments 0, -1, and +1 are shown in Figures 2, 3, and 4 respectively. The flat fields are similar at other energies, except for the UVIS structure at low energies. The gradient in QE in the dispersion direction of all three segments can clearly be seen. This gradient is present at all energies and is not mimicked in the HRC-I flat field calibrations (which indicates that it was not an artifact of the experimental setup and intrinsic to the detector). Additionally, there is a region of segment +1 that has a slightly lower gain and QE. The tabulated QE of the central segment was determined for a 9.46 mm (V axis) by 5.35 mm (U axis) region centered on the optical center of the detector. The entire region is under the thick Al coating of the central UVIS (i.e. no UVIS boundaries were crossed).

Two proportional counters (PC) were used for absolute normalization of the beam. A beam normalization detector (BND) could be inserted and withdrawn via a vacuum feedthrough directly between the X-ray source and the HRC. The BND and the HRC were never run simultaneously because of the proximity of the two detectors and a slow gas leak through the thin BND window. A monitor detector (MD) was placed at 90 degrees to the beam to monitor temporal variations. The take-off angle between the electron impact source and either proportional counter was 45 degrees, so the intensity at either detector should be the same, assuming that the beam filters are identical. We do not rely on this assumption, however. Our calibration technique was to simultaneously illuminate the BND and MD to make an absolute measurement of the X-ray intensity and cross-calibrate the two proportional counters. The HRC and MD were then illuminated.

The dead time in the HRC becomes significant at rates above a few hundred cts/s. The HRC electronics are non-paralyzable with an event processing time of 68.5 μs. The true rate, r_t, is given by

$$r_t = \frac{r_m}{1 - \tau r_m}, \tag{1}$$

where r_m is the measured HRC-S rate (cts/s) over the entire detector, and τ is the event processing time. The dead time correction ranges from 2% for the O K_α measurements to 10% for the Al K_α measurements. All flat field QEs have been dead time corrected.

The measured HRC-S QEs rely on the BND QEs, and any error in the BND QE will translate directly into an error in the measured HRC-S QE. The transmission of the PC windows was measured at a several energies. The thickness of the window was determined by fitting a simple slab absorption model via non-linear regression to this data. The absorption of the PC gas (P-10 or methane) was calculated using the physical depth of the counter, the measured pressure and temperature of the gas, and the Henke mass absorption coefficients.

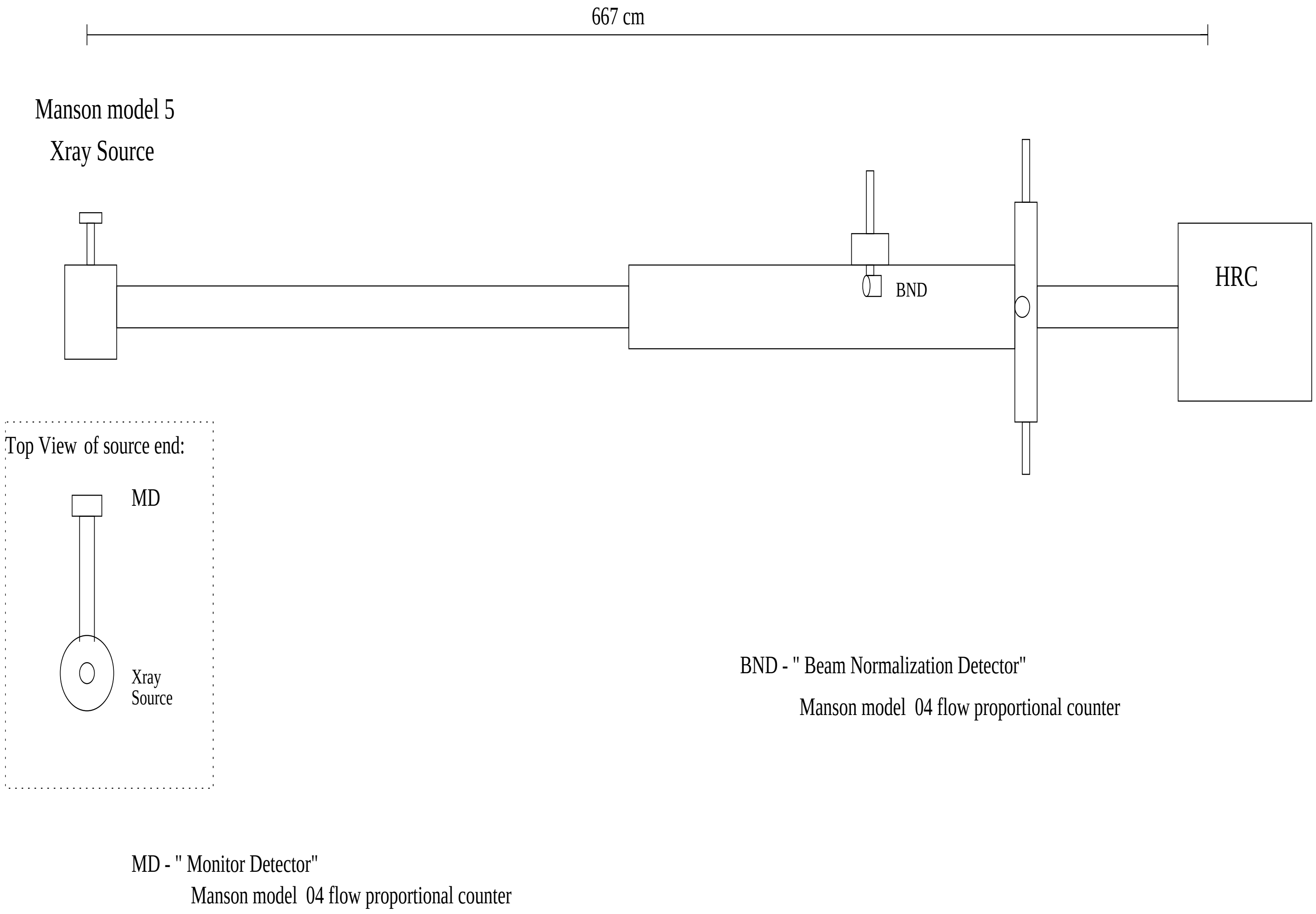

Figure 1: Schematic diagram of experimental setup for HRC flat field measurements.

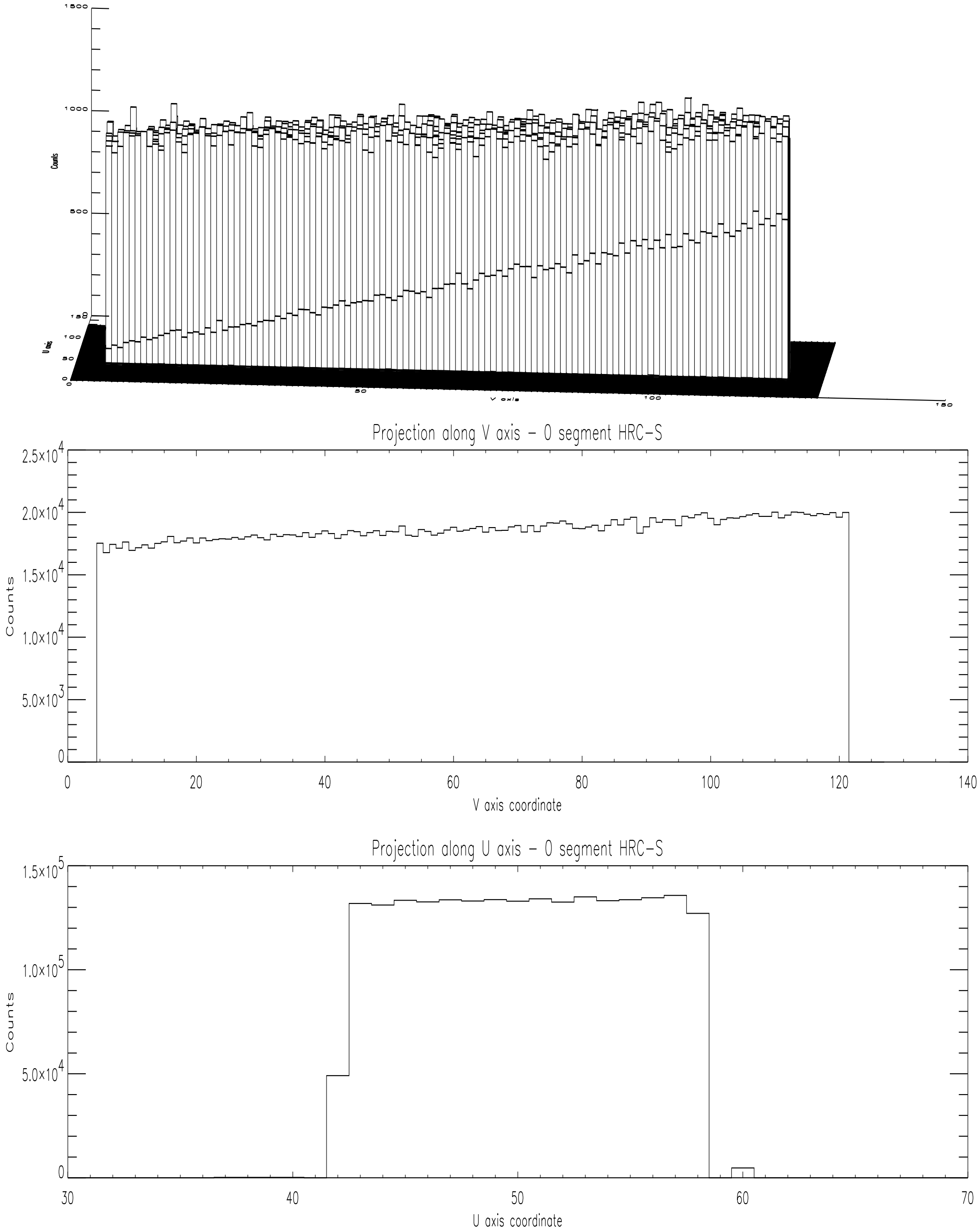

Figure 2: Surface plot and projections along U and V axes of HRC-S segment 0, Al K_{α}. Each pixel is 0.82 μm.

These counters have not been cross-calibrated against any other detector, nor have they been calibrated at a synchrotron. Although we rely heavily on this flat field data for our QE calibration, our uncertainties in our overall calibration are not dominated by the systematics at these few flat field energies. As described below, we do not have enough measurements of the QE at enough energies below 1.5 keV. Even if these detectors were now cross-calibrated against, say, one of the MST BNDs or taken to BESSY for a detailed calibration, it would not significantly change the overall uncertainties of the HRC-S calibration.

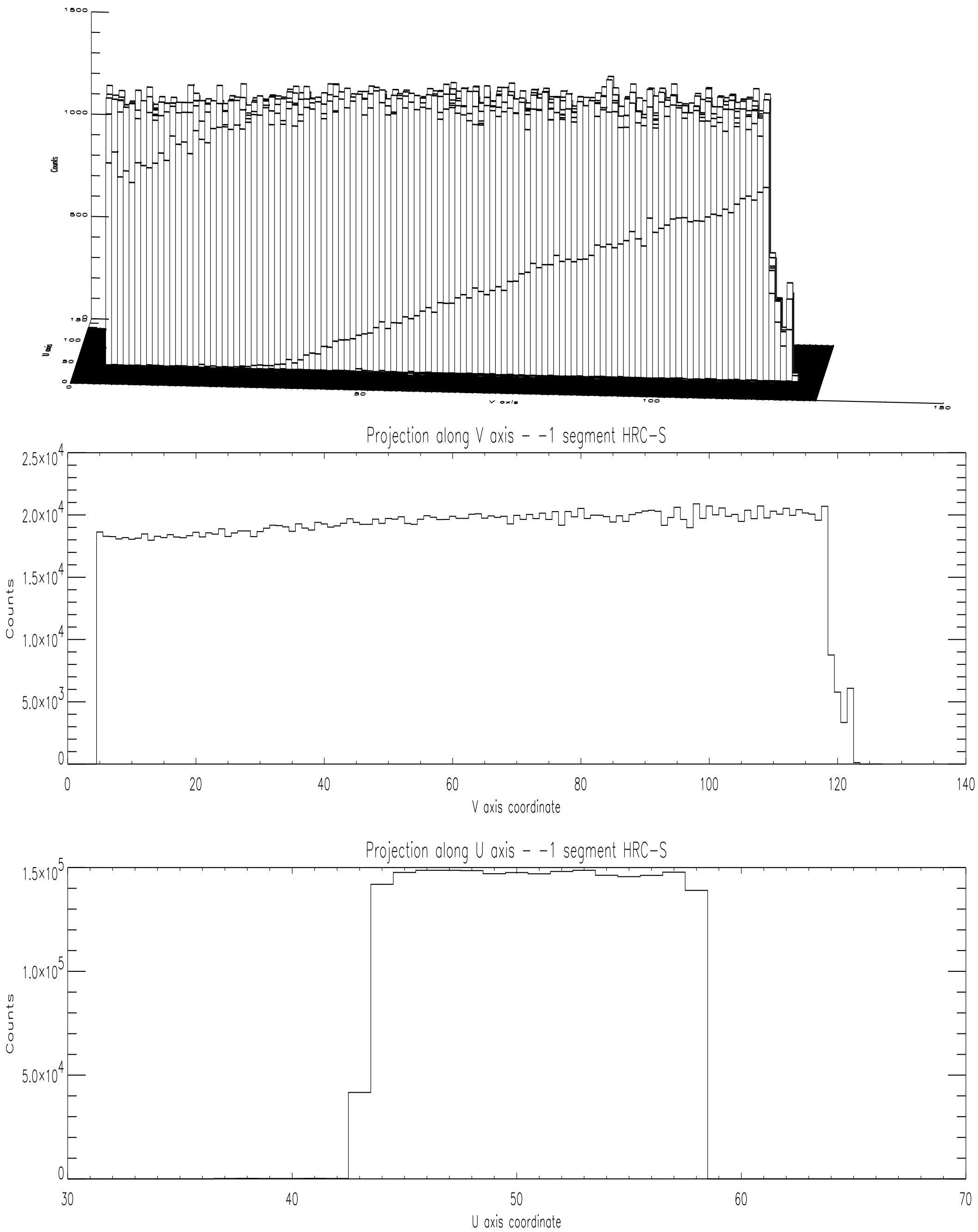

Figure 3: Surface plot and projections along U and V axes of HRC-S segment -1, Al K_α. Each pixel is 0.82 μm.

The spectral purity of several of the anodes used in the flat field measurements is relatively low. For the Ti K_α and Fe K_α measurements, there are actually 2 strong lines (K_α and K_β), as well as the bremsstrahlung continuum. A thick filter of the same material as the anode was used to filter out the continuum, but this will have the additional effect of further enhancing the flux in the K_β line relative to the K_α line at the detector. Therefore the assumption of a single monochromatic line is not valid. This problem is most severe for the Ti measurement because the Ti K_α line is on the low energy side of the I L_{III} edge, and the K_β line is above the edge. The MCP QE jumps by approximately a factor of 2 across the edge. The strength of the K_α line relative

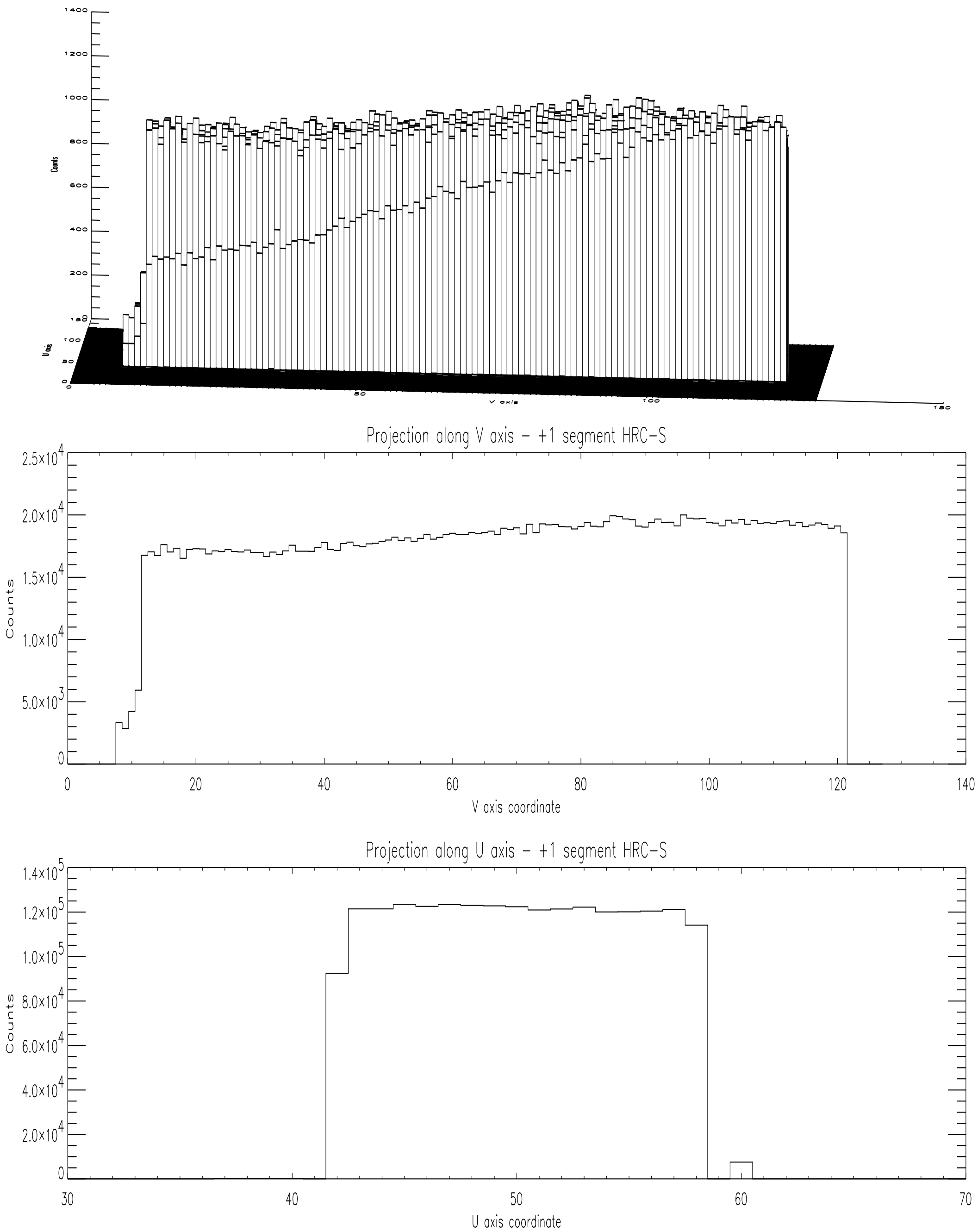

Figure 4: Surface plot and projections along U and V axes of HRC-S segment +1, Al K_α. Each pixel is 0.82 μm.

to the K_β line can be seen in the CCD spectrum of the Ti anode and Ti filter shown in Figure 5. No detector features are located between the Fe K_α and K_β line, so we would expect that this error would be smaller for the Fe flat field.

We can make a quantitative estimate of this error. Assume that the incident spectrum consists of two spectral lines (i.e. ignore the continuum). The ratio of the flux in the K_β line to K_α line, λ, can be computed

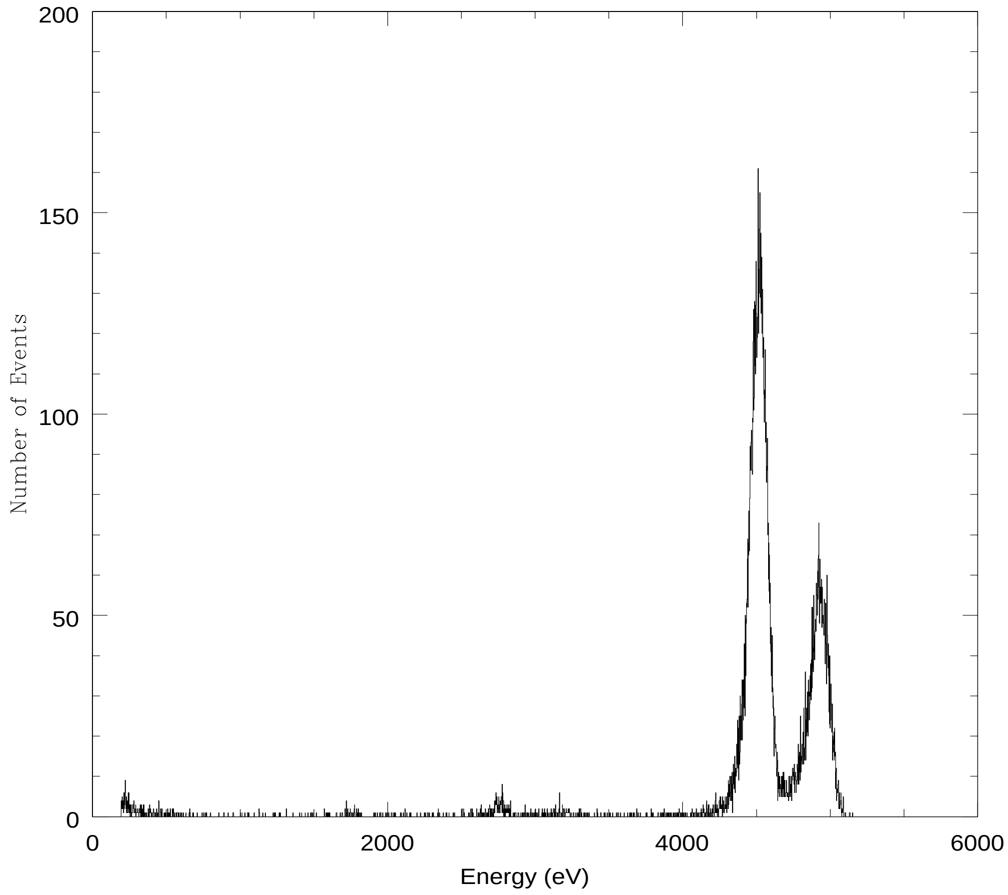

Figure 5: CCD spectrum of X-ray emission from Ti anode and 125 μm filter.

from the fluorescent yields and the transmissions of the appropriate filters. The calculated ratio is 0.54 for the Ti measurement and 0.57 for the Fe measurement. The CCD spectrum can be used to place a lower limit on this ratio which is consistent with the calculated ratio in both cases. Therefore, under the assumption of monochromaticity, we would make an incorrect estimate of QE at the primary line (the K$_\alpha$ line), Q_1^{MCP}, by a factor f which is given by

$$f = \frac{1 + \lambda \frac{Q_2^{pc}}{Q_1^{pc}}}{1 + \lambda \frac{Q_2^{MCP}}{Q_1^{MCP}}}, \tag{2}$$

where Q_2^{MCP} is the MCP QE at the secondary (K$_\beta$) line, Q_1^{pc} is the PC QE at the primary line, and Q_2^{pc} is the PC QE at the secondary line. From the DCM measurements, we have a good estimate of the ratio of the MCP QE at the two lines of interest. By assuming a monochromatic spectrum, we would overestimate the QE at Fe K$_\alpha$ by 4% and by 18.5% at Ti K$_\alpha$. These corrections have been applied to the data.

The Ni L flat field measurement also has a low line to continuum ratio. The continuum was filtered with a thin Cu foil. This source spectrum consists of the Ni L$_\alpha$ line at 851 eV, a weaker L$_\iota$ line at 743 eV, and continuum from ~700 eV to the Cu L_{III} edge at 929 eV and above 1500 eV to 2500 eV (the anode voltage. The continuum between the Ni L$_\alpha$ line and the Cu L_{III} edge can clearly be seen in the two CCD spectra shown in Figure 6. The spectrum shown as the solid line is a spectrum taken with the Ni anode an Cu filter (identical to the HRC-S FF). The spectrum shown as the dashed line was taken using a Ni anode, but with a Ni filter instead of the Cu filter. The energy resolution of the detector is ∼60 eV FWHM. The continuum contamination on both sides of the main spectral line is significant. The error in the QE is not as easy to estimate since it depends in a complex fashion on the true source spectrum, the energy dependence of the PC QE, and the energy dependence of the MCP QE. The MCP QE, in particular, is complex in this spectral region around the Cs and I M edges. For this measurement, there could be a significant (10-15%) systematic error due to this complex source spectrum. Detailed spectral fitting of the PC spectrum or, preferably, the CCD spectrum is required for a quantitative estimate.

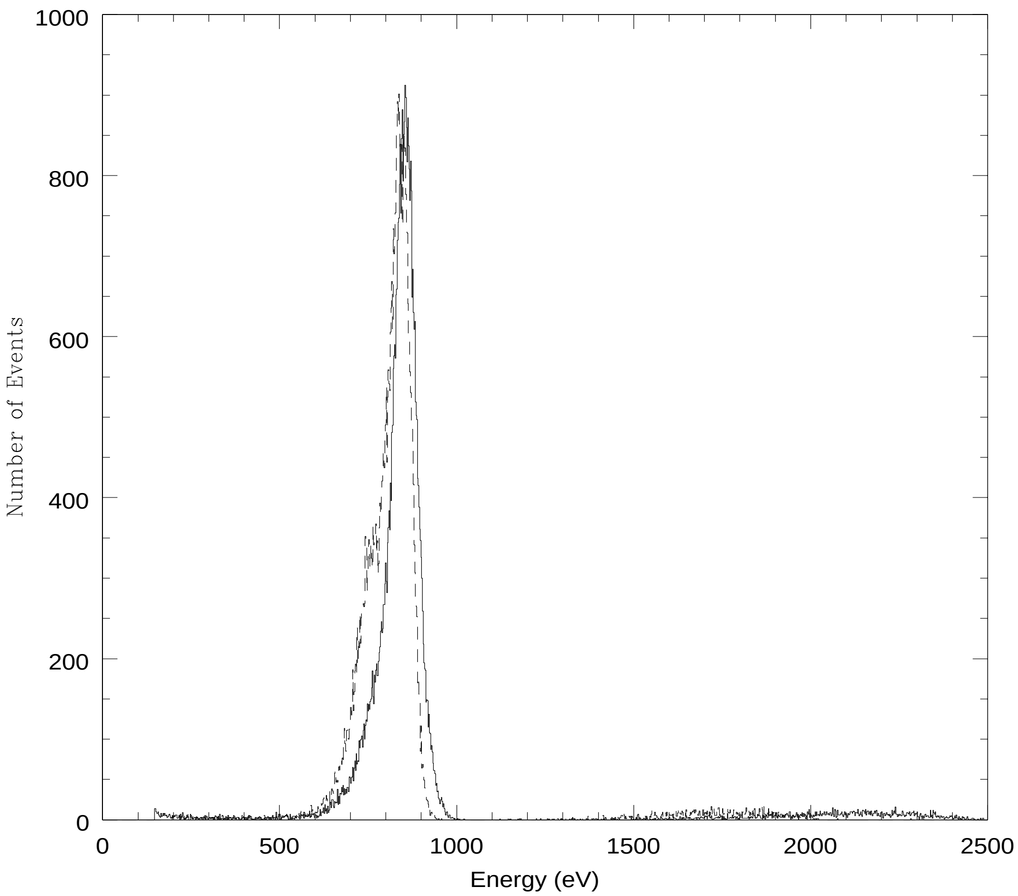

Figure 6: Two CCD spectra of X-ray emission from Ni anode. The solid line was taken with a 2 μm Cu source filter (identical to the FF measurement) and the dashed spectrum was taken with a 2 μm Ni source filter. Note the bremsstrahlung continuum between the Ni L_α line and the Cu L_{III} edge, and above 1500 eV.

As described earlier in this report, the QE of the HRC-S changed significantly when the electronic modifications were made after XRCF. A plot of the ratio of pre-fix QE to post-fix QE versus energy in a region around the center of the central segment is shown in Figure 7. A cubic spline has been fit to the data points to provide a continuous estimate of the fractional change in QE as a function of energy. The endpoints were chosen arbitrarily to ensure that the spline fit was well behaved at ends of the CXO bandpass. It is necessary to apply this correction to all XRCF EA measurements around zeroth order to adjust them to the flight configuration. Given the large spatial non-uniformities in the pre-fix configuration, the data and curve shown in Figure 7 are not necessarily representative of the change in QE over the entire detector. Most of the spatial non-uniformity present in the detector at XRCF has been removed (see above). Note the apparent bump in the spline fit above ∼700 eV. This is the region around the Cs and I M edges and it is clear from the pulse height distributions that above about 500 eV, the PHDs become more skewed to higher pulse heights. The low QE at XRCF was caused by a combination of the low MCP gain and thresholds, and it is therefore reasonable to expect that if the gain changed in a complex manner with energy after the electronic modifications, the QE could also change in a complex manner, hence the complex shape of this curve.

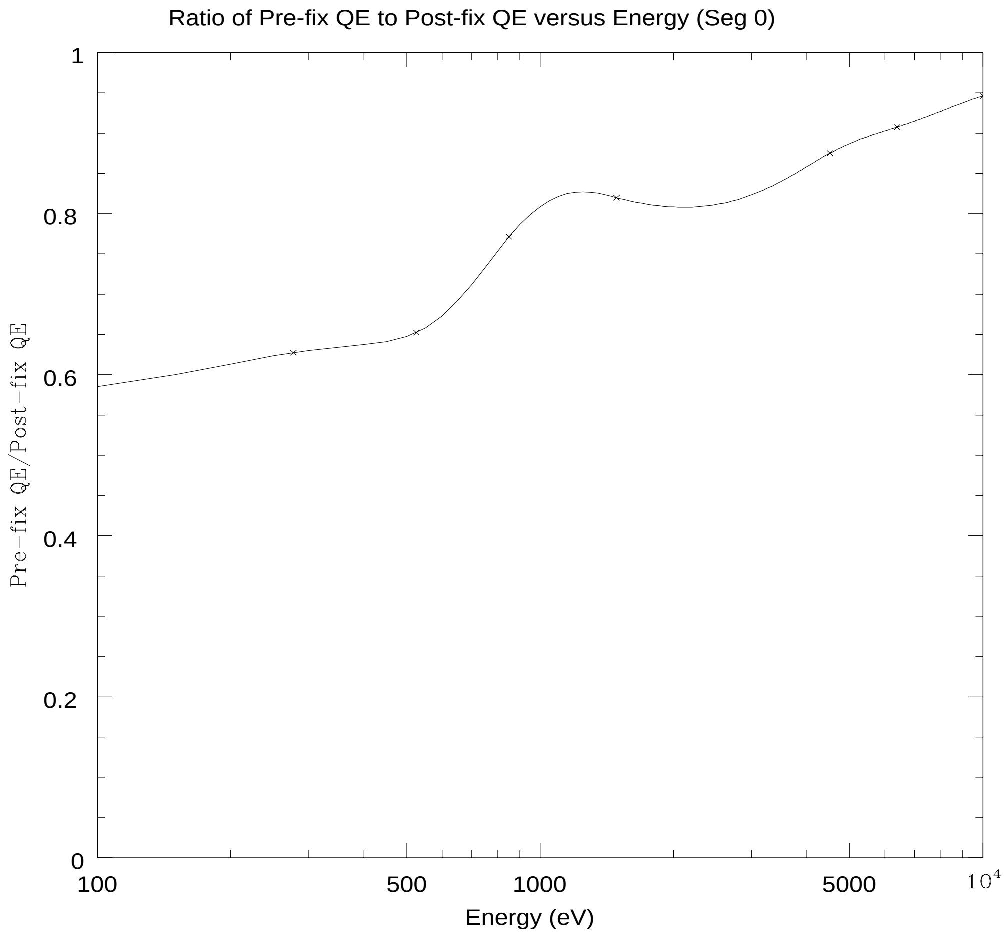

Figure 7: Ratio of pre-fix QE to post-fix QE versus energy in a region around the zeroth order position.

The HRC-S QE measurements made at XRCF and the QE measured in flat fields around zeroth order are plotted in Figures 8 and 9 along with statistical error bars. The Xs with errorbars are the HIREFS points, the open boxes with the error bars are the DCM points, and the open pentagon with error bars is the EIPS measurements. The open triangles with no error bars are the flat field QE measurements. There are no error bars on these points because the statistical error bars are insignificant compared to the systematic uncertainties. Note the progressively larger errorbars at lower energies for the HIREFS data. As described above, we consider only the HIREFS data above 1.5 keV to be reliable for use in the absorption model.

A summary of the measurements of the MCP QE of the HRC-S in a region around zeroth order as a function of energy that we have used for interpolation in the absorption model is given in Table 2. The origin (SAO FF, DCM, EIPS, or HIREFS) of each point is also listed. We have guided the interpolation so that the derived QE curve in is well behaved regions where we don't have enought reliable data (i.e. between the C K_α and O K_α measurements, and just below the I L_{III} edge).

From 1.5 keV to 10 keV, we have a considerable number of points each with a small (few percent) statistical error. The DCM measurements agree to within $\sim$10% with the SAO FF QE measurements, which is probably

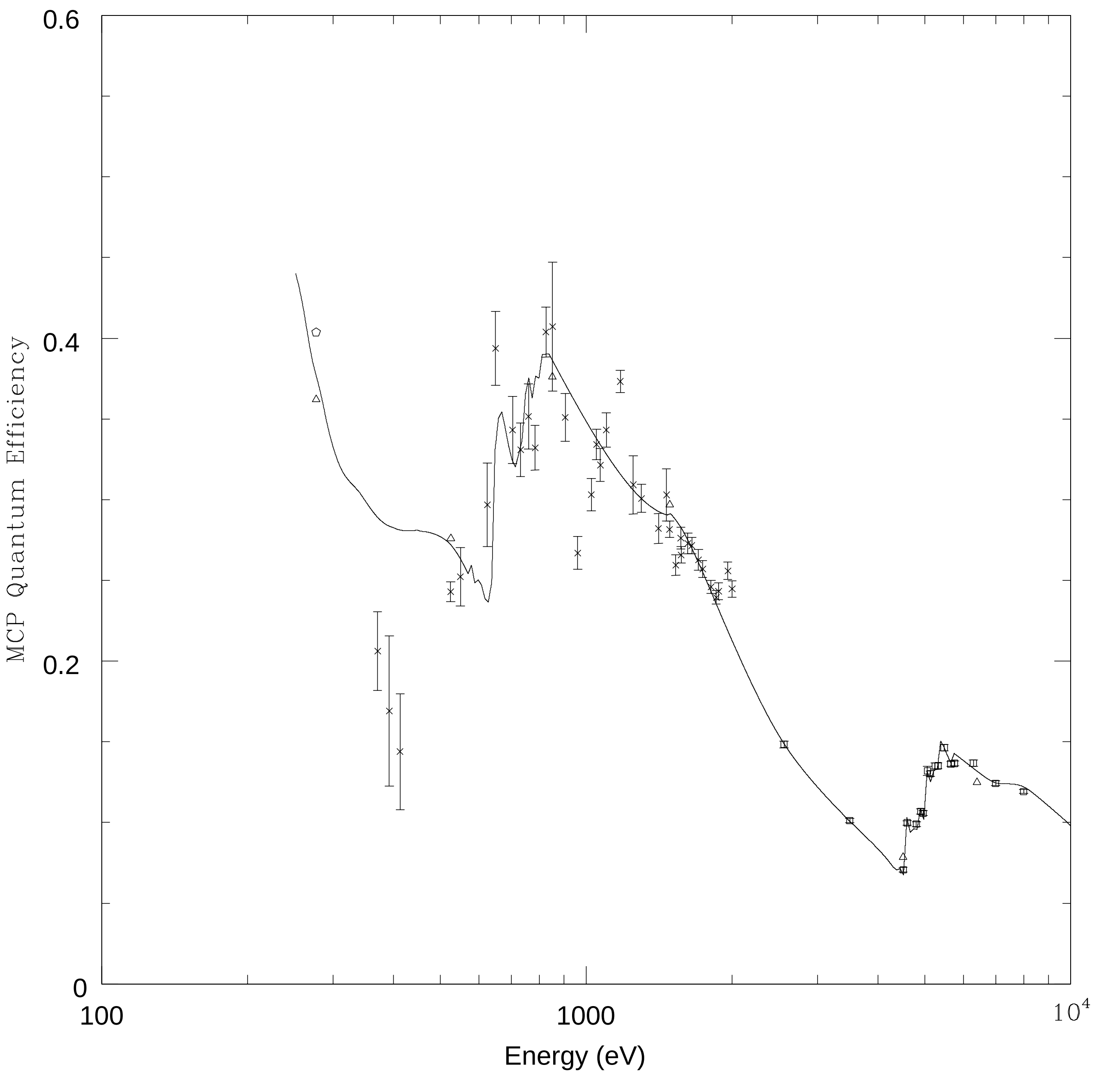

Figure 8: MCP QE of HRC-S in a region around the zeroth order. The Xs with errorbars are the HIREFS points, the open boxes with the error bars are the DCM points, and the triangles with error bars are the EIPS measurements. The open triangles with no error bars are the SAO flat field QE measurements.

a good measure of the systematic uncertainty in this bandpass. Between 277 eV and 1487 keV, however, the only reasonably reliable QE measurements are the 4 SAO FFs and one XRCF EIPS measurement! This is, in our opinion, the major source of uncertainty in the HRC-S QE calibration below 1.5 keV. We do not have QE measurements at enough energies to adequately constrain the shape of the QE versus energy curve. We have synchrotron measurements of the QE between 600 eV and 800 eV that are described in detail below, but it is

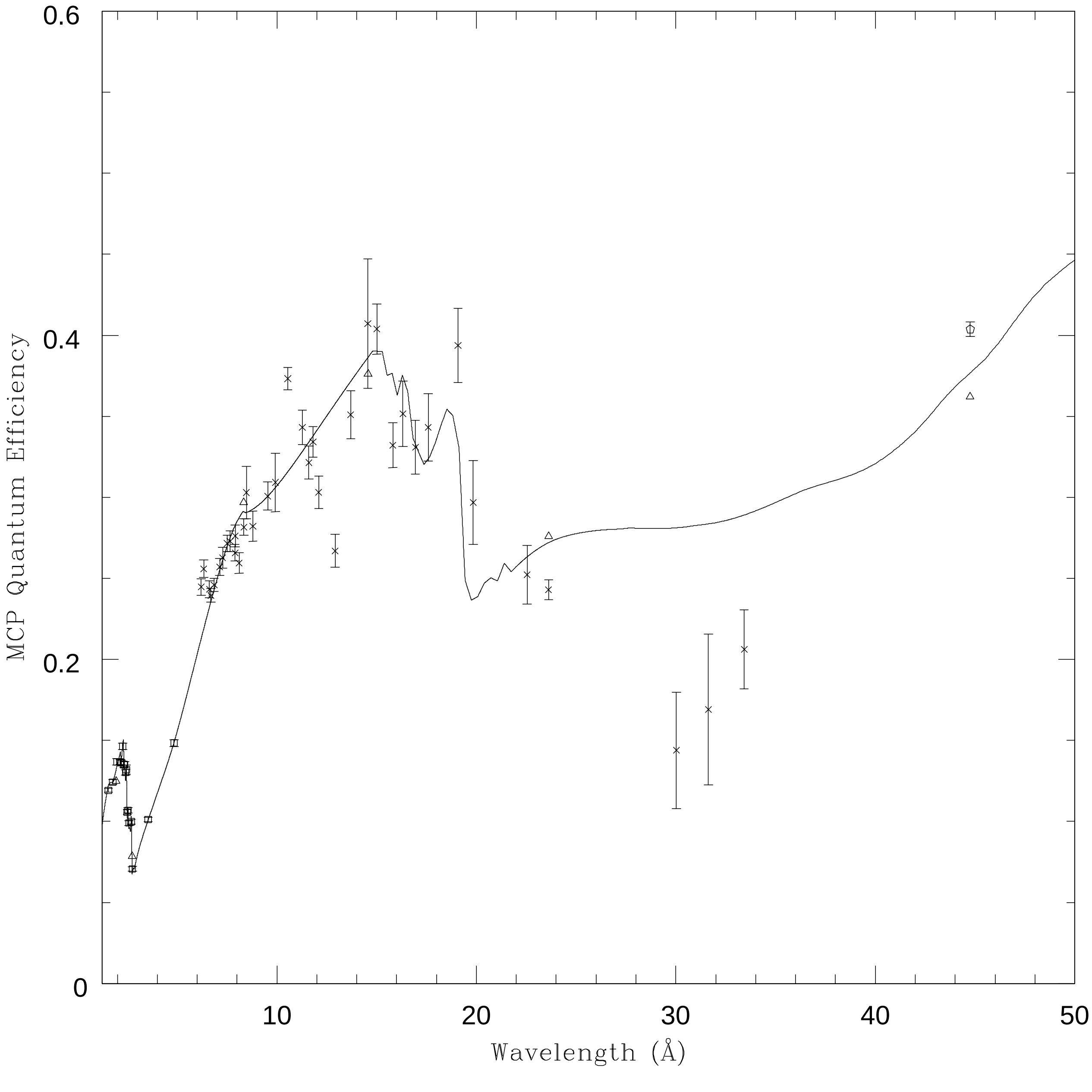

Figure 9: MCP QE versus wavelength in zeroth order. The is the same as Figure 8 except that the QE is plotted versus wavelength.

not a straightforward problem to combine this data with the data on the flight instrument. Below 277 eV, the only data we have are the SAO FF and an XRCF EIPS QE measurement at 183 eV, as well as synchrotron measurements on CsI coated MCPs. These three measurements at the low energy end of the bandpass are not self-consistent. We therefore conclude that we can not say anything quantitative below 277 eV until we observe the low energy calibration targets (e.g. HZ 43) in orbit and make further measurements of the soft X-ray response of CsI coated MCPs in the HRC laboratory.

Energy (eV)	QE (Measured)	Origin	Uncertainty
277.	0.370	SAO FF and XRCF EIPS	(0.10)
525.	0.276	SAO FF	(0.10)
851.	0.376	SAO FF	(0.12)
1487.	0.297	SAO FF	(0.10)
1652.	0.272	HIREFS	0.0052
1855.	0.239	HIREFS	0.0043
2560.	0.152	DCM	0.0021
3500.	0.101	DCM	0.0014
4510.	0.0709	DCM	0.0015
4600.	0.101	DCM	0.0014
4800.	0.0997	DCM	0.0015
4900.	0.108	DCM	0.0017
4960.	0.106	DCM	0.0015
5060.	0.131	DCM	0.0028
5130.	0.130	DCM	0.0018
5250.	0.134	DCM	0.0019
5320.	0.134	DCM	0.0017
5480.	0.147	DCM	0.0020
5660.	0.137	DCM	0.0014
5760.	0.143	DCM	0.0015
6300.	0.137	DCM	0.0019
7000.	0.126	DCM	0.0015
8000.	0.125	DCM	0.0013

Table 2: Summary of HRC-S calibration data points. These are the energies and QEs that are used in the absorption model, as well as the uncertainty. For the DCM and HIREFS measurements, the uncertainty is entirely statistical. For the SAO FF measurements, the statistical uncertainties are negligible, so we have included an estimate of the systematic uncertainty.

1.3 MCP QE Absorption Model - interpolation to a finer energy scale

A semi-empirical model outlined in a memo by M. Juda (1997) was used to generate the interpolated MCP QE over a finer energy mesh in the 277 eV to 10000 eV bandpass. The model will be summarized here in detail for completeness. It is assumed that the QE of CsI coated MCPs, Q_{MCP}, can be described by a function of the form

$$Q_{MCP} = f(1 - exp(-y(E))), \tag{3}$$

where f is the open area fraction of the MCPs (0.58), and y is the electron yield, that is, the average number of photo-electrons generated by an X-ray of energy E that escape the CsI and are accelerated down the pore to record a detectable event. The MCP QE is therefore given by f times one minus the probability that an event creates no electrons with are detected. We assume that the yield, $y(E)$, is given by

$$y(E) = \Lambda(E)\rho_{CsI}\mu(E)_{CsI}, \tag{4}$$

where $\Lambda(E)$ is an 'electron range' parameter (units of cm), ρ_{CsI} is the mass density of CsI, and $\mu(E)_{CsI}$ is the mass absorption coefficient of CsI. The parameter $\Lambda(E)$ contains all of the complex physics of the initial charge generation and electron transport. It is expected that Λ is a weak function of E, so that the MCP QE is governed primarily by the absorption properties of CsI. There is experimental evidence that this model is a reasonable representation of the response of photocathodes (Henke, Knauer, and Premaratne 1981).

Given the measured QEs from Table 2, Λ can be found at each energy by inverting Equation 4. A spline curve is fit to the measured Λ at a much finer energy grid, and $Q_{MCP}(E)$ is then computed by inserting the empirically determined $\Lambda(E)$ back into Equation 4. The 1993 Henke mass absorption coefficients for Cs and I are used. This model provides a reasonable approximation to the data except around the M absorption edges. Based on a comparison with synchrotron measurements, this model overestimates the jump ratio at the M (and L) absorption edges and positions the M edges at the wrong energies. The displacement of the M edges of high-Z materials from previously tabulated values has been seen in reflectivity measurements and is understood (see, for example, Owens, *et al.*, 1996). Since the jump ratio at the M edges is overestimated, the shape of the curve above the edge is also incorrect.

Synchrotron measurements of the QE of CsI coated MCPs in the 600 eV to 1200 eV bandpass were made in $\sim$0.5 eV energy steps. A complete discussion of the synchrotron measurements is given in Rideout, *et al.*, 1998. Unfortunately, the results of the synchrotron measurements cannot be combined with the XRCF and SAO FF QE data in a straightforward manner because the absolute QE of the synchrotron data is considerably higher than that measured for the flight instrument, and there is no cross-calibration between the two datasets. The reason for this difference is unknown. The absorption model is clearly inadequate around the Cs and I M edges for the reasons discussed above, so it is important to find an improved model in this bandpass. We have chosen to subtract a constant scaling factor from the synchrotron data to make it consistent with the SAO FF data at the O K_α calibration point. While this is clearly an ad-hoc procedure, the resulting QE curve does have the edges at the correct energy and the jump ratios across the edges are smaller than predicted by the interpolation algorithm. There is clearly considerable uncertainty in this procedure, but it provides a more appropriate treatment around the absorption edges. A second order polynomial was used to model the QE between the 851 eV calibration point and the 1487 eV point to better match the structure in this spectral region than the absorption model. We hope to better constrain the shape of the QE curve is this region with additional measurements in the HRC laboratory.

The curve overplotted on the datapoints in Figures 8 and 9 is the MCP QE curve derived from the combination of the absorption model and the synchrotron data. As can be seen from the Figure, the model *qualitatively* describes the HIREFS data below 1.5 keV which was not used in generating the model. We recognize the inadequacy of the data and model below 1 keV. To address this problem, we are currently making additional measurements of the QE of CsI coated MCPs in the HRC laboratory to further understand the shape of the QE curve below 1 keV.

1.4 HRC-S QE in 0th, 1st, 3rd, and 5th Orders of the LETG

The QE of the HRC-S (i.e. MCP QE times UVIS transmission) in zeroth order is shown in Figures 10 and 11. The transmission of the UVIS has been well calibrated as described in section TBD, so the uncertainties are dominated by the uncertainties in the MCP QE. Some of the important features in the QE curve have been labeled (Not YET TBD). An additional correction was applied to the MCP QE to account for incident angle effects and the integrated HRMA cone angles. This correction is larger than 1% only below 400 eV (see section TBD for complete discussion). The effective area of the HRMA + HRC-S on-axis is shown in Figure 12.

It is necessary to consider several additional spatial effects to determine the QE of the HRC-S at the position where a given energy and order is dispersed to including the normalization between the segments, the QE gradient across each segment, and the complex structure of the UVIS, and the position and width of the gaps between each segment. Based on the SAO FF measurements, the QE of the two wing segments is $\sim$10% lower at all energies than the central segment. We also made flat field measurements of the QE of the wing segments. The results of these measurements are summarized in Table 3. There is also a gradient in QE across each segment. The magnitude of this gradient is $\sim$10% between the maximum value to minimum value for a given segment. A schematic diagram of the UVIS is given in Figure TBD. The exact positioning of the various segments, gaps, the UVIS, the center of the central segment, and the optical axis is discussed in section TBD. The HRC-S QE in the 1st, 3rd and 5th orders of the LETG is shown in Figures 13, 14, and 15 versus energy, and in Figures 16, 17, and 18 versus wavelength, respectively. Data tables of the data contained in these plots

Line	Energy	QE (+1 segment)	QE (-1 segment)
C K_α	277 eV	0.230	0.235
O K_α	525 eV	0.187	0.183
Al K_α	1487 eV	0.297	0.295

Table 3: Measured HRC-S QE (UVIS not divided out) for the two wing segments.

are attached in the appendix at the end of the document.

1.5 Uncertainty in the Quantum Efficiency Calibration and Future Work

As described throughout, the major uncertainty in the QE calibration of the HRC-S is the QE of the MCP. Above 1.5 keV, the HRC-S was well calibrated at XRCF, and one can extrapolate this calibration to the current flight configuration. The differences in QE between the XRCF measurements and the SAO FF measurements give a quantitative limit on the systematic uncertainty in the HRC-S QE of ∼10%. The systematics of the DCM calibrations are probably better than this. We estimate ∼7% uncertainty in the HRC-S QE above 1.5 keV. Below 1.5 keV, however, we just do not have reliable measurements of the QE at enough energies to constrain it to better than ∼15% except near the few calibration points. The response of the HRC-S below 200 eV is effectively uncalibrated.

We do have an extensive on-orbit calibration program that includes an extended observation of HZ 43, and a several cross-calibration observations with ACIS/HETG. The HZ 43 observation will allow us to constrain the low energy QE to the accuracy of the models of white dwarf atmospheres (∼15%), and the ACIS/HETG cross-calibrations will allow us to further constraint the QE in the 400 eV - 1500 eV bandpass.

We are also making additional detailed measurements of the QE of CsI coated MCPs in the HRC laboratory to better define the shape of the QE curve in the 70 eV to 1000 eV bandpass. We are using a reflection grating monochromator to provide a spectrally pure beam in a manner similar to that used to measure the transmission of the UVIS witness samples. Initially we will use K, L, and M emission lines from a variety of low Z anodes in combination with the grating to provide a spectrum of high spectral purity. We also plan to use the continuum generated from a Ta anode so that we can use the system as a true monochromator and provide 'dial-up' energies. Our X-ray CCD camera will be used to verify the spectral purity of all measurements.

2 Pulse-Height Distributions

The HRC-S has some limited intrinsic (i.e. non-dispersive) energy resolution. The SAO FF data used for the QE and uniformity measurements described above was also used to quantify the non-dispersive energy resolution of the HRC-S. The PHD was measured at 7 energies for the central segment (183 eV, 277 eV, 525 eV, 851 eV, 1487 eV, 4510 eV, and 6404 eV), and 4 energies (183 eV, 277 eV, 525 eV, and 1487 eV) for each of the wing segments. Figures 19, 20, and 21 contain the pulse-height distributions for the center (only 5 of the 7 energies are shown), +1, and -1 segments, respectively. These PHDs have not been background subtracted. The small feature below channel 30 in most of the PHDs is due to the background. For the PHDs at 183 eV, this background is significant because of the low rate from the source.

Several features are immediately obvious from the distributions. First, between 183 eV and 1487 eV, the centroid of the distribution increases with increasing energy. Above 1487 eV, however, there is little or no energy dependence to the centroid. Second, the PHDs get progressively broader with increasing energy. For the two highest energy measurements, there is a considerable tail at large pulse heights. The combination of these two features could be used to extract some spectral information about a source.

In an effort to quantify the PHDs, we have made an estimate of the background, subtracted it from the PHDs, then fit the product of two Gaussians (via non-linear regression) to the distributions. The function form of the fit is given by

$$P_i = \frac{N_1}{\sqrt{2\pi}\sigma_1} e^{-(\frac{c_i - C_1{}^2}{2\sigma_1^2})} + \frac{N_2}{\sqrt{2\pi}\sigma_2} e^{-(\frac{c_i - C_2{}^2}{2\sigma_2^2})}, \tag{5}$$

where P_i is the normalized value for the c_ith channel, the Ns are the relative weights of the two Gaussians, the Cs are the centroids, and the σs are the widths. The parameters of the double Gaussians for each segment at each of the calibration energies is tabulated in Table 4.

Energy	Segment	N_1	C_1	σ_1	N_2	C_2	σ_2
277 eV	0	0.74	83.95	15.11	0.26	80.58	29.07
525 eV	0	0.72	88.87	15.40	0.28	96.74	29.19
851 eV	0	0.68	95.79	15.58	0.32	109.76	31.50
1487 eV	0	0.57	95.71	16.43	0.43	117.42	31.84
4510 eV	0	0.48	95.75	17.07	0.52	126.88	40.52
6404 eV	0	0.37	96.23	17.38	0.63	129.25	43.01
277 eV	+1	0.64	76.89	15.92	0.36	85.27	26.59
525 eV	+1	0.67	81.79	16.24	0.33	94.87	28.24
1487 eV	+1	0.59	88.73	17.49	0.41	112.90	32.12
277 eV	-1	0.53	95.00	14.19	0.47	96.06	29.46
525 eV	-1	0.58	100.38	15.72	0.42	109.71	31.47
1487 eV	-1	0.52	108.72	17.42	0.48	131.56	38.37

Table 4: Best fit parameters of double Gaussian fit to HRC-S pulse-height distributions.

3 References and General Bibliography

- Henke, B. L., Gullikson, E. M., and Davis, J. C., Atom. Data and Nucl. Data Tables, **54**(2), 181, JUL93.
- Juda, M., "A Simple Model for the QE of CsI coated MCPs", SAO Internal Memo, 1997.
- Kenter, A. T. *et al.*, "Performance and Calibration of the AXAF High Resolution Camera I: Imaging Readout", *EUV, X-Ray, and Gamma-Ray Instrumentation for Astronomy VIII*, O. H. W. Siegmund and M. A. Gummin, eds., Proc. SPIE 3114, 1997.
- Kenter, A. T., "HRC QE versus angle of incidence", SAO Internal Memo, September 1998.
- Kolodziejczak, J. J., Austin, R. A., Elsner, R. F., Joy, M. K., Sulkanen, M. E., Kellogg, E. M., and Wargelin, B. J., *X-ray and Extreme Ultraviolet Optics*, R. B. Hoover and A. B. Walker, eds., Proc. SPIE 2515, 1995.
- Kraft, R. P., Chappell, J. H., Kenter, A. T., Kobayashi, K., Meehan, G. R., Murray, S. S., Zombeck, M. V., Fraser, G. W., Pearson, J. F., Lees, J. E., Brunton, A. N., and Pearce, S. E., *EUV, X-Ray, and Gamma-Ray Instrumentation for Astronomy*, O. H. W. Siegmund and M. A. Gummin, eds., Proc. SPIE 2808, 1996.
- Kraft, R. P. *et al.*, "Performance and Calibration of the AXAF High Resolution Camera II: Imaging Readout", *EUV, X-Ray, and Gamma-Ray Instrumentation for Astronomy VIII*, O. H. W. Siegmund and M. A. Gummin, eds., Proc. SPIE 3114, 1997.

- Meehan, G. R. *et al.*, "Calibration of the UV/Ion Shields for the AXAF High Resolution Camera", *EUV, X-Ray, and Gamma-Ray Instrumentation for Astronomy VIII*, O. H. W. Siegmund and M. A. Gummin, eds., Proc. SPIE 3114, 1997.
- Murray, S. S. *et al.*, "The AXAF High Resolution Camera (HRC): Calibration ad Recalibration at XRCF and Beyond", *EUV, X-Ray, and Gamma-Ray Instrumentation for Astronomy VIII*, O. H. W. Siegmund and M. A. Gummin, eds., Proc. SPIE 3114, 1997.
- Owens, A., S. C. Bayliss, P. J. Durham, S. J. Gurman, and G. W. Fraser, *Ap. J.*, **468**, 451, 1996.
- Patnaude, D. *et al.*, "Effective Area of the AXAF High Resolution Camera (HRC)", *EUV, X-Ray, and Gamma-Ray Instrumentation for Astronomy VIII*, O. H. W. Siegmund and M. A. Gummin, eds., Proc. SPIE 3445, 1998.
- Pearce, S. E., Lees, J. E., Pearson, J. F. Fraser, G. W., Brunton, A. N., Flanagan, K. A., Kenter, A., Barbera, M., Dhanak, V., Robinson, A., and Teehan, D., *EUV, X-Ray, and Gamma-Ray Instrumentation for Astronomy VI*, O. H. W. Siegmund and J. V. Vallerga, eds., Proc. SPIE 2518, 1995.
- Rideout, R. A. *et al.*, "Synchrotron Measurements of the Absolute X-ray Quantum Efficiency of CsI-coated Microchannel Plates", *EUV, X-Ray, and Gamma-Ray Instrumentation for Astronomy VIII*, O. H. W. Siegmund and M. A. Gummin, eds., Proc. SPIE 3445, 1998.

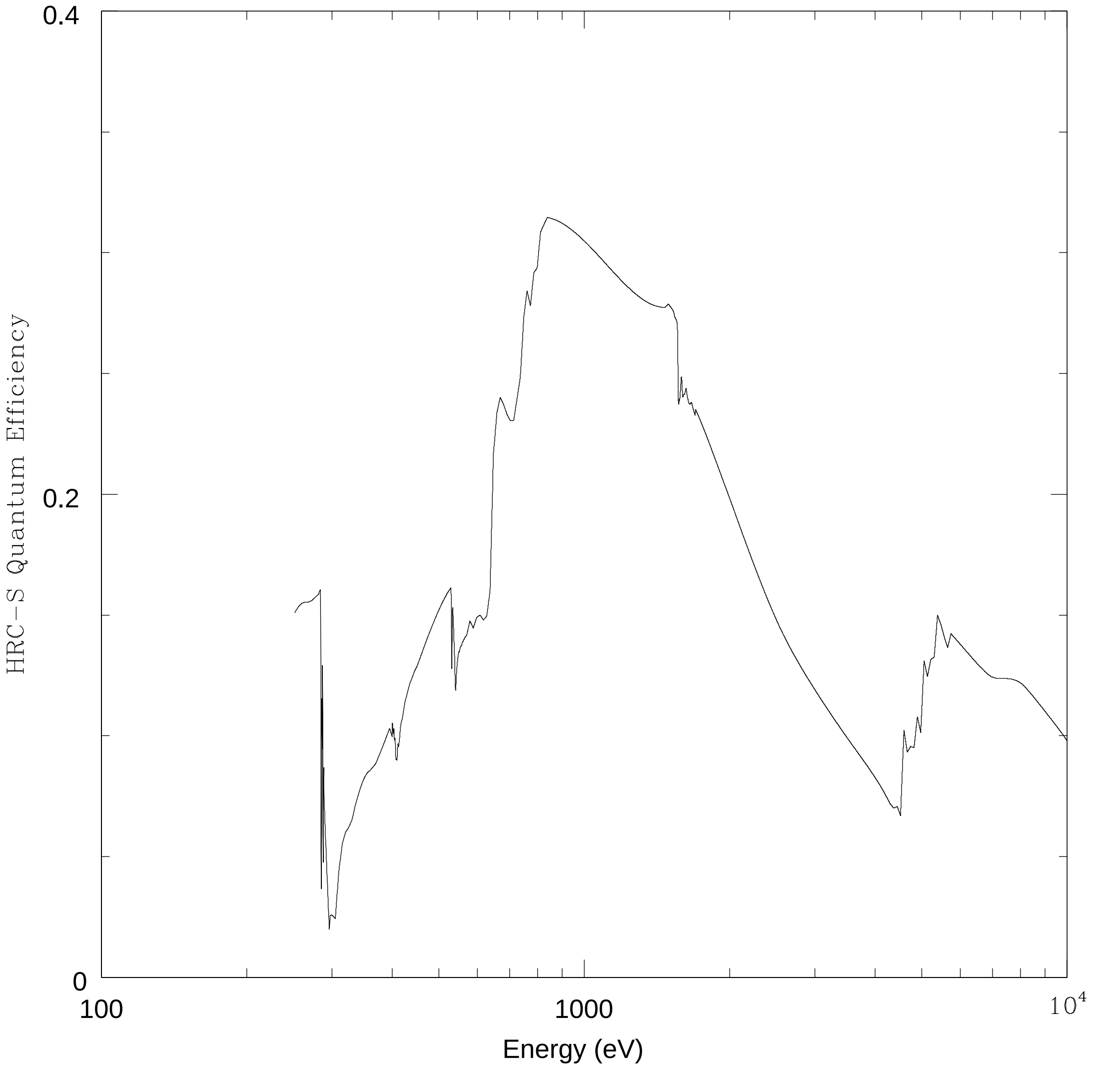

Figure 10: QE of HRC-S (MCP QE and UVIS transmission) versus energy in zeroth order.

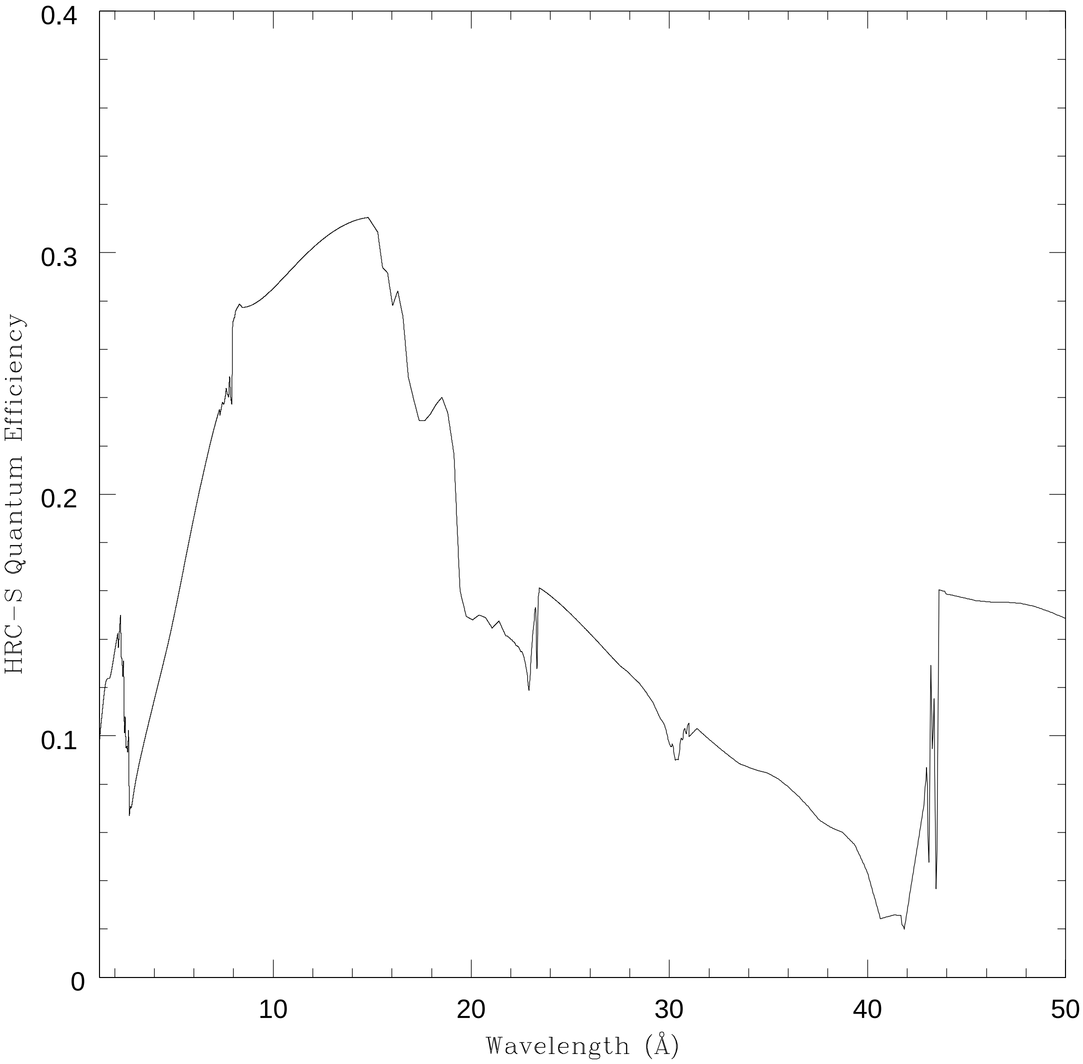

Figure 11: QE of HRC-S (MCP QE and UVIS transmission) versus wavelength in zeroth order.

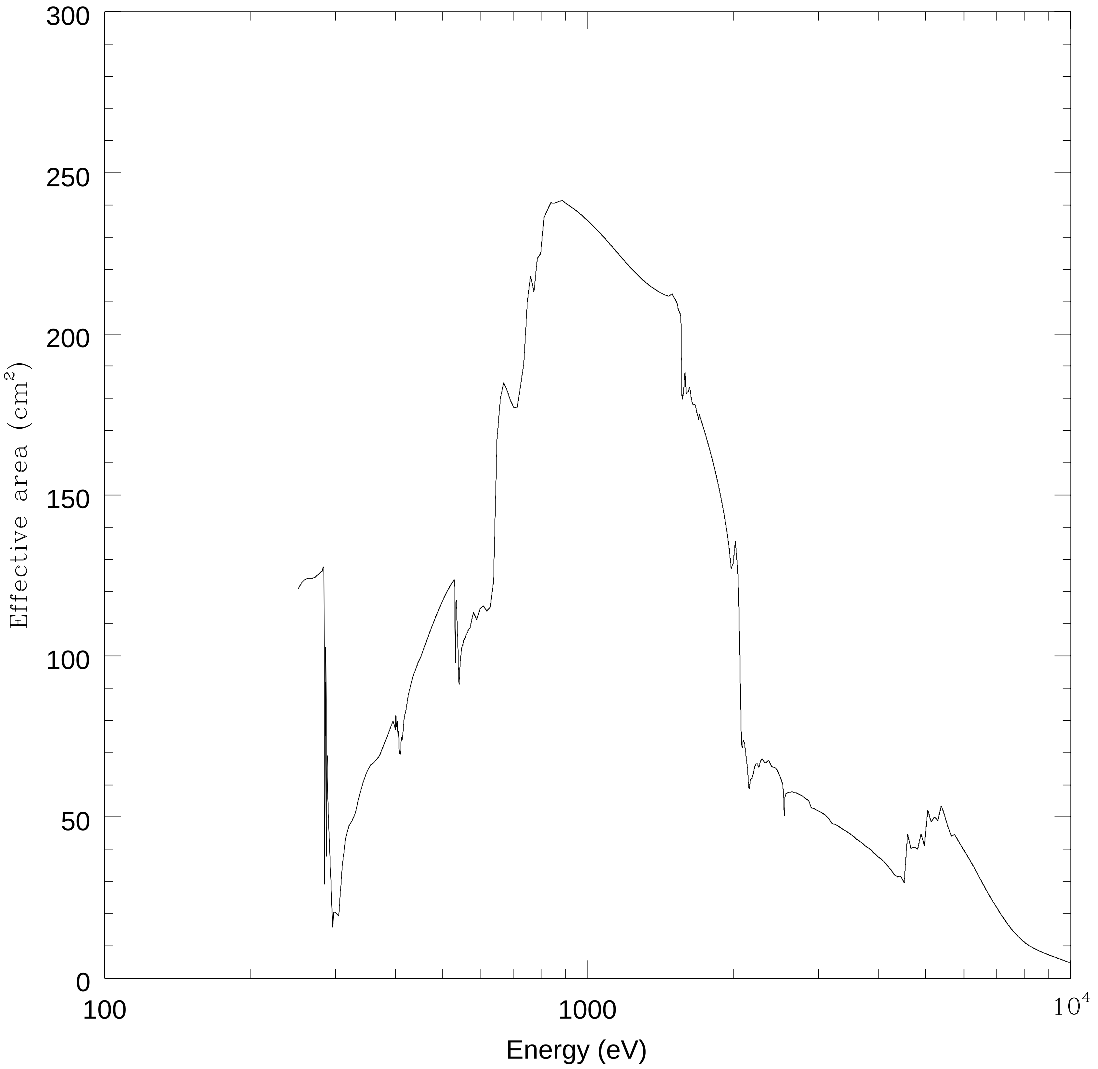

Figure 12: Effective area of HRC-S + HRMA on-axis.

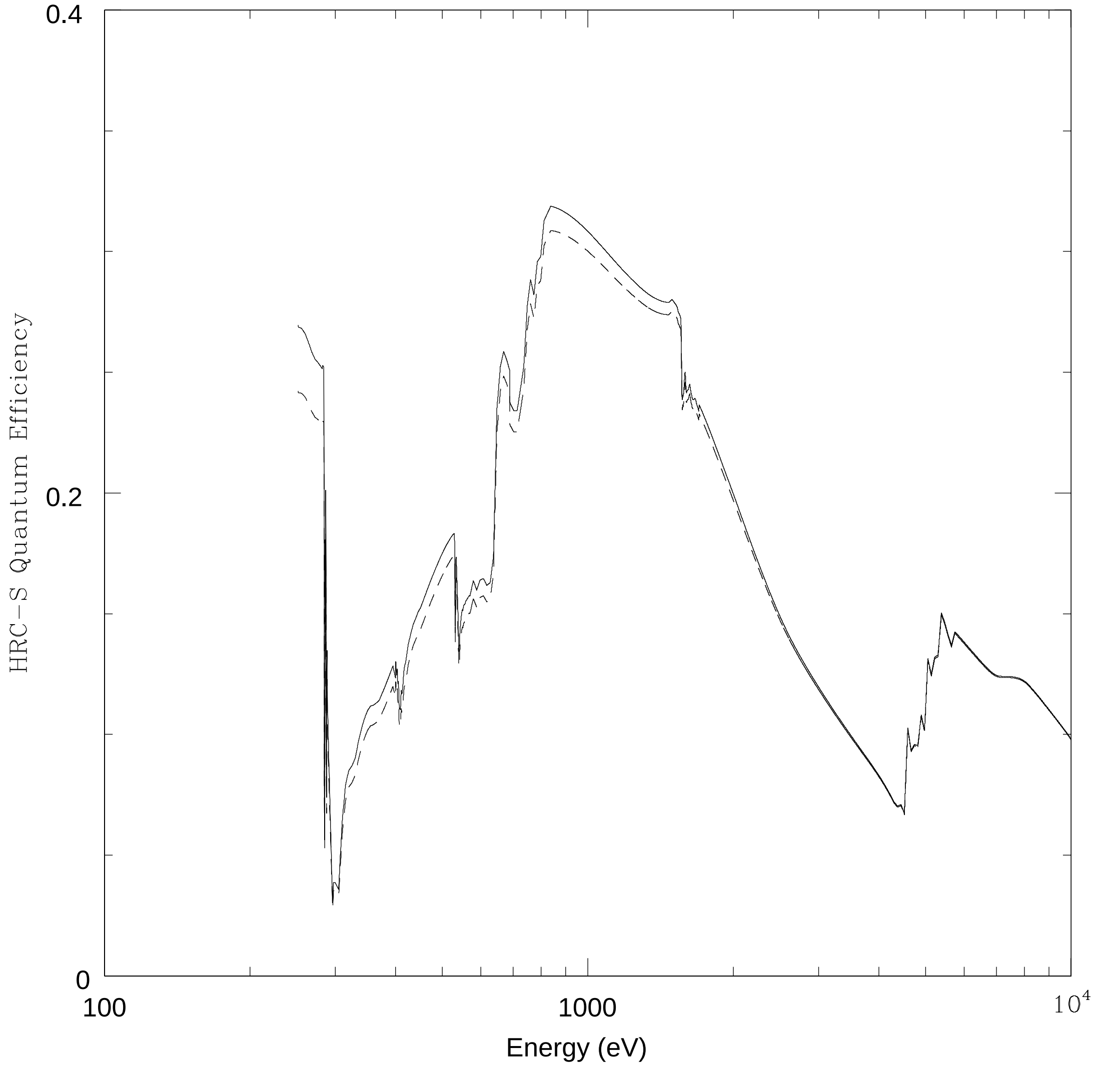

Figure 13: QE of HRC-S (MCP QE and UVIS transmission) in 1st order of the LETG (i.e. QE of the HRC-S at the position where the first order at energy E is dispersed by the LETG) versus energy. The solid curve is the -1 order, the dashed curve is the +1 order.

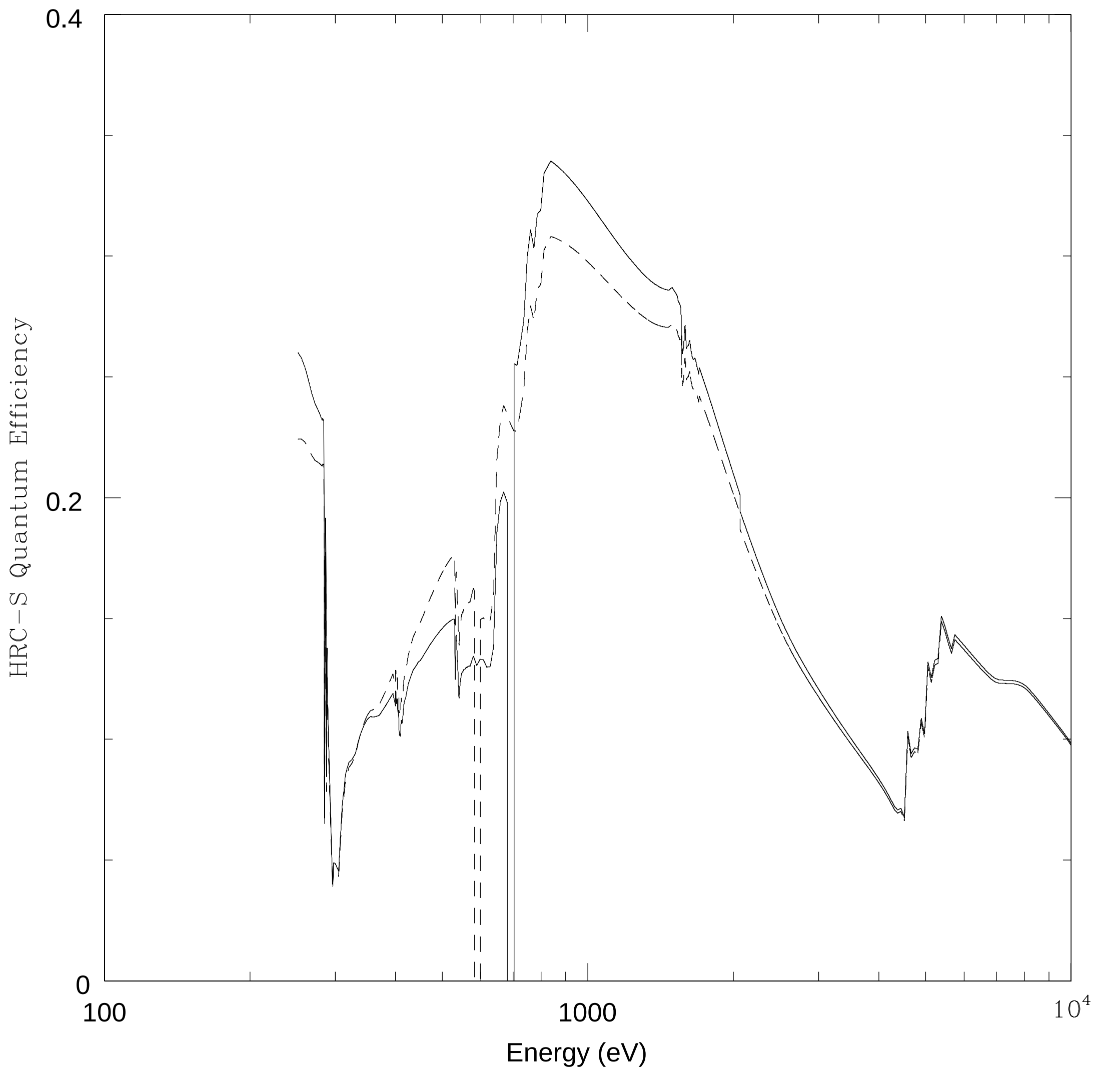

Figure 14: QE of HRC-S (MCP QE and UVIS transmission) in 3rd order of the LETG (i.e. QE of the HRC-S at the position where the third order at energy E is dispersed by the LETG) versus energy. The solid curve is the -3 order, the dashed curve is the +3 order.

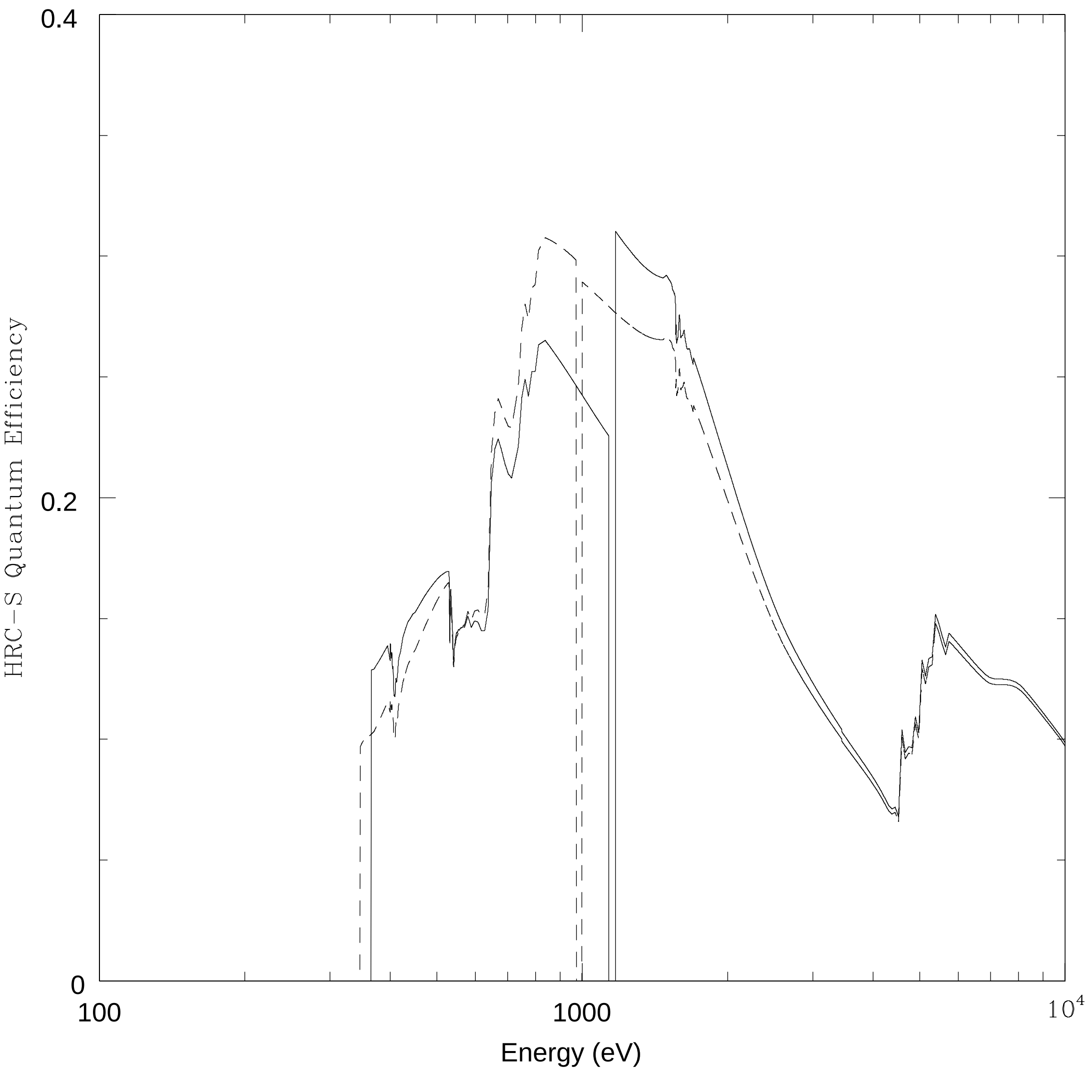

Figure 15: QE of HRC-S (MCP QE and UVIS transmission) in 5th order of the LETG (i.e. QE of the HRC-S at the position where the fifth order at energy E is dispersed by the LETG) versus energy. The solid curve is the -5 order, the dashed curve is the +5 order.

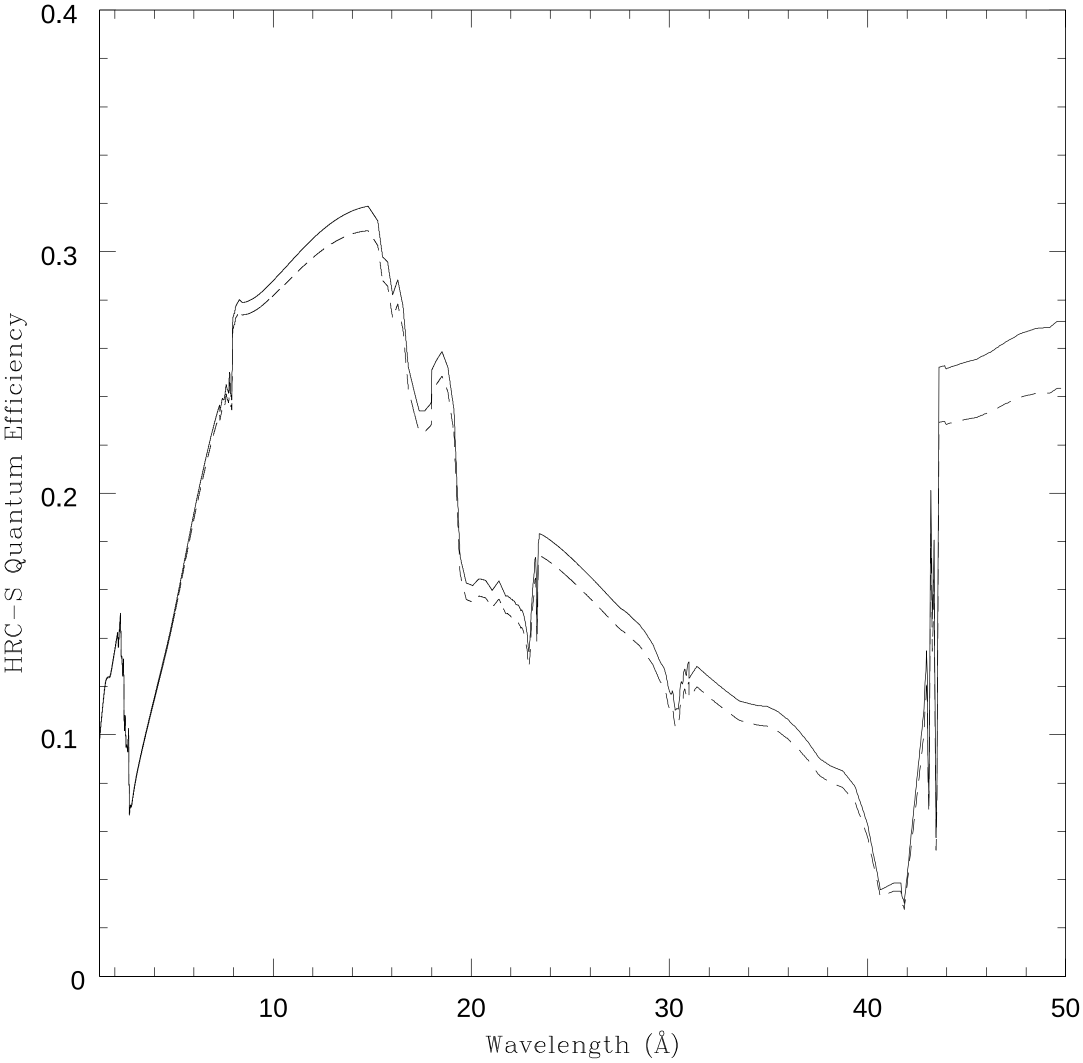

Figure 16: QE of HRC-S (MCP QE and UVIS transmission) in 1st order of the LETG (i.e. QE of the HRC-S at the position where the first order at wavelength λ is dispersed by the LETG) versus wavelength. The solid curve is the -1 order, the dashed curve is the +1 order.

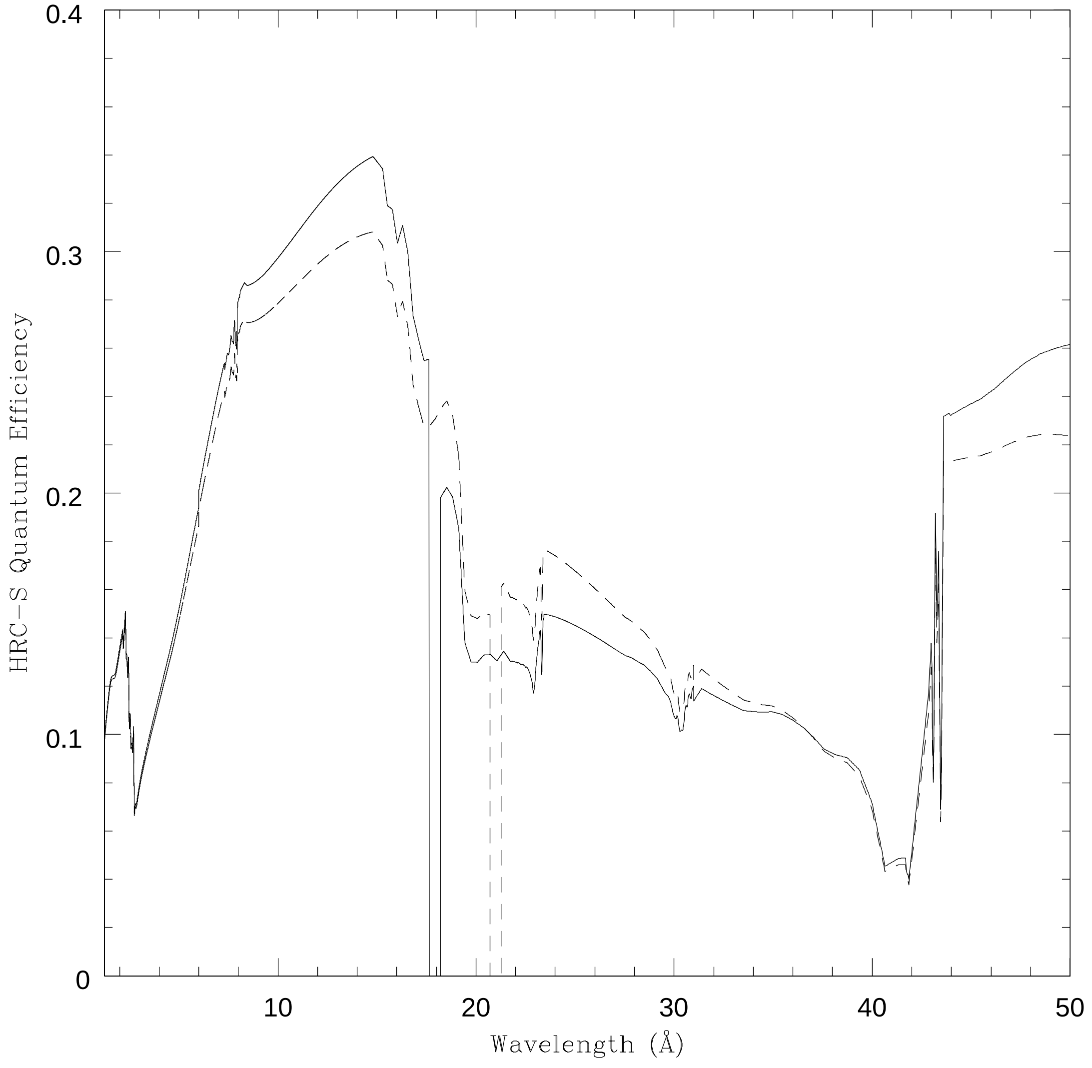

Figure 17: QE of HRC-S (MCP QE and UVIS transmission) in 3rd order of the LETG (i.e. QE of the HRC-S at the position where the third order at wavelength λ is dispersed by the LETG) versus wavelength. The solid curve is the -3 order, the dashed curve is the +3 order.

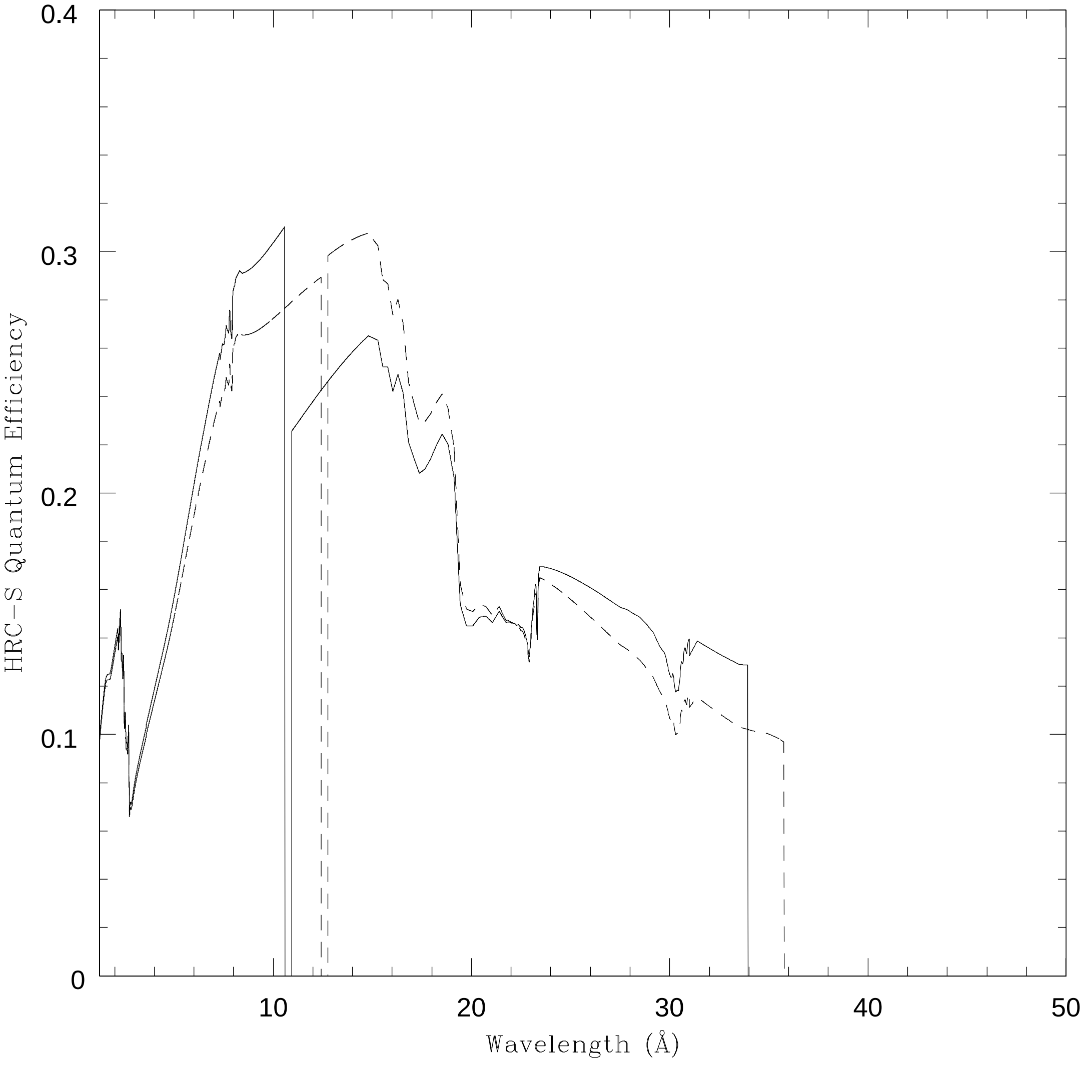

Figure 18: QE of HRC-S (MCP QE and UVIS transmission) in 5th order of the LETG (i.e. QE of the HRC-S at the position where the fifth order at wavelength λ is dispersed by the LETG) versus wavelength. The solid curve is the -5 order, the dashed curve is the +5 order.

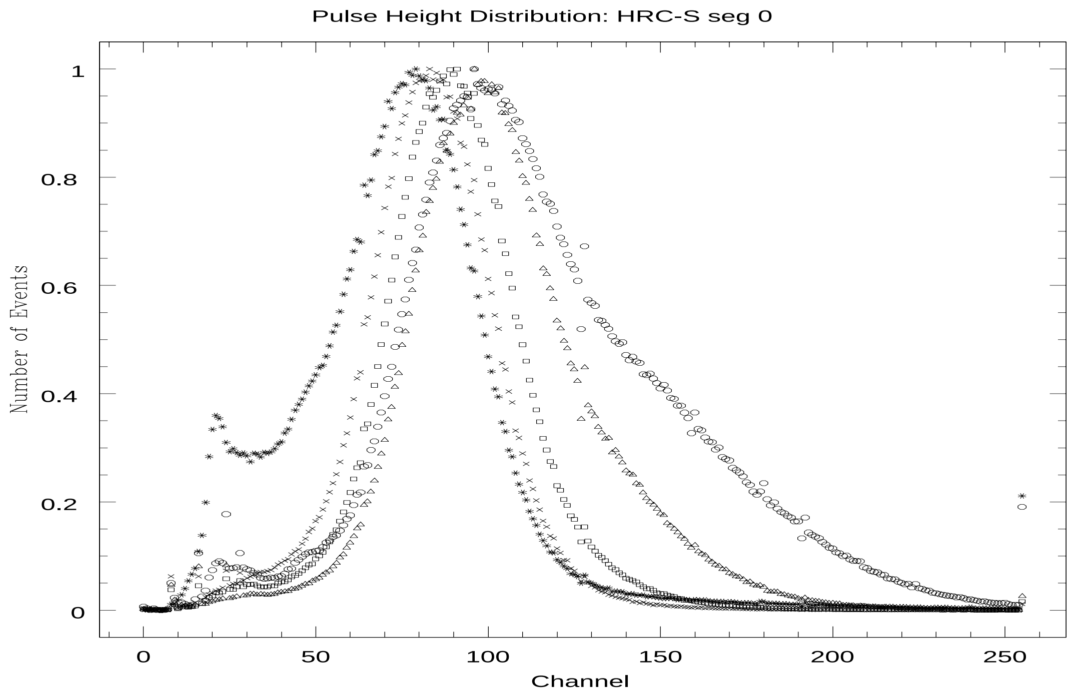

Figure 19: Pulse height distributions of the central segment of the HRC-S at five energies. The asterisks are the PHD at 183 eV, the Xs at 277 eV, the squares at 525 eV, the triangles at 1487 eV, and the cirles at 6404 eV.

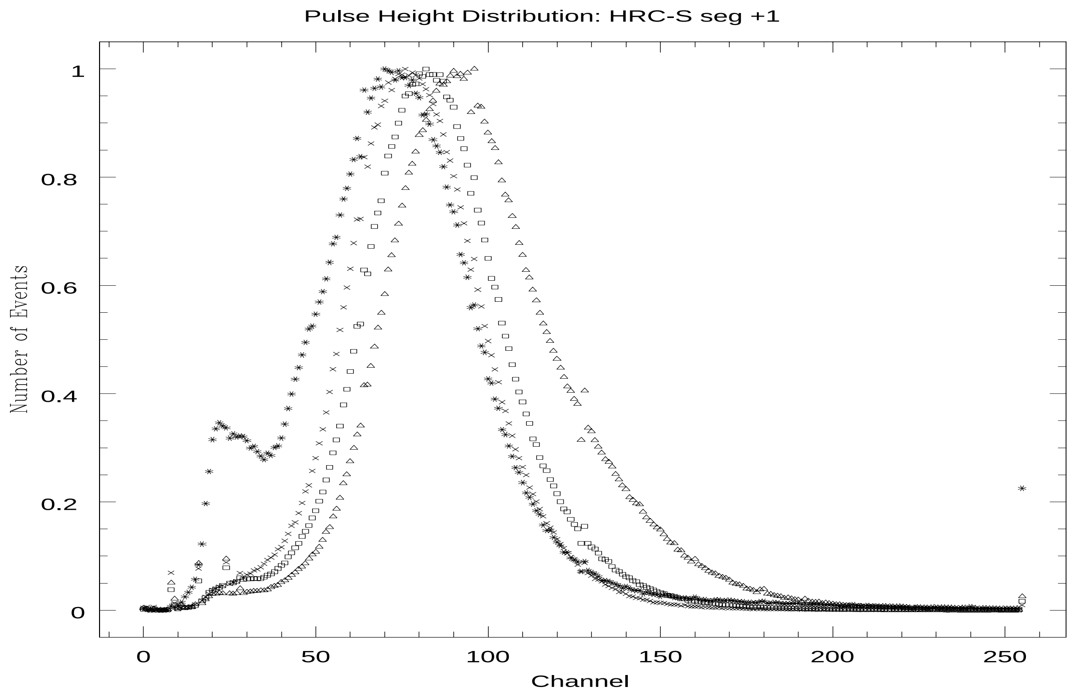

Figure 20: Pulse height distributions of the +1 segment of the HRC-S at four energies. The asterisks are the PHD at 183 eV, the Xs at 277 eV, the squares at 525 eV, and the triangles at 1487 eV.

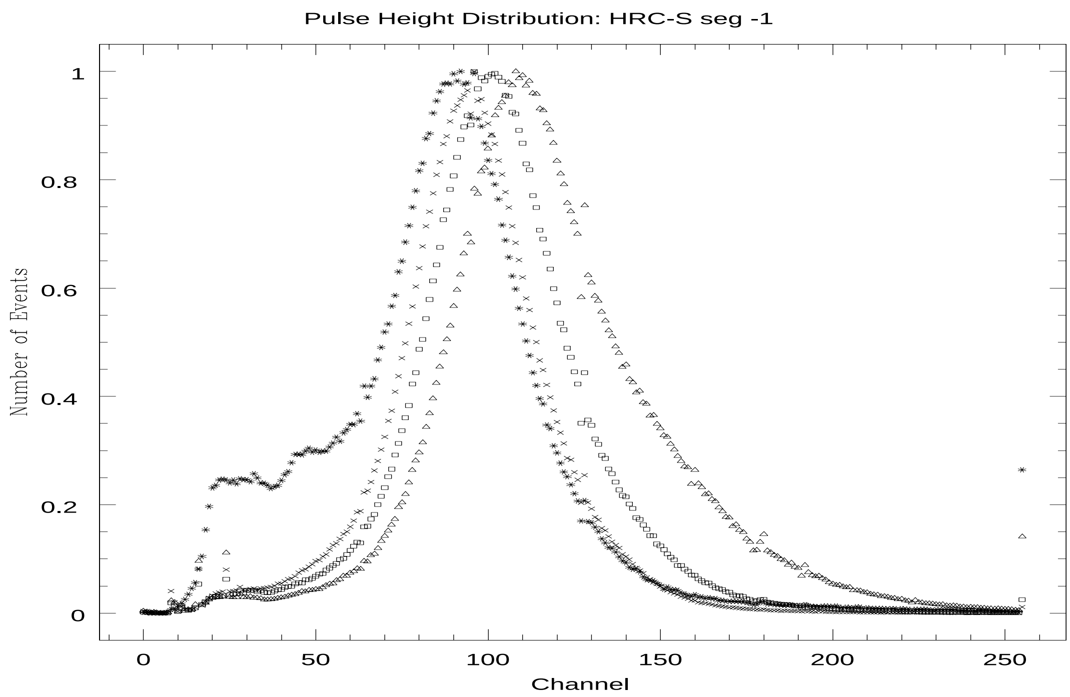

Figure 21: Pulse height distributions of the -1 segment of the HRC-S at four energies. The asterisks are the PHD at 183 eV, the Xs at 277 eV, the squares at 525 eV, and the triangles at 1487 eV.